

# Strain and foliation refraction patterns around buckle folds

MARCEL FREHNER<sup>1\*</sup> & ULRIKE EXNER<sup>2,3</sup>

<sup>1</sup>*Geological Institute, ETH Zurich, Sonneggstrasse 5, 8092 Zurich, Switzerland*

<sup>2</sup>*Department for Geodynamics and Sedimentology, University of Vienna, Althanstrasse 14, 1090 Vienna, Austria*

<sup>3</sup>*Natural History Museum, Burgring 7, 1010 Vienna, Austria*

\*Corresponding author (e-mail: marcel.frehner@erdw.ethz.ch)

**Abstract:** Axial plane foliation associated with geological folds may exhibit a divergent or convergent fan. Commonly, the foliation is assumed to reflect the major principal finite strain orientation. Here, the strain orientation around numerically simulated single-layer buckle folds is analysed in detail. Four different strain measures are considered: (1) finite strain, (2) infinitesimal strain, (3) incremental strain (recording the strain history from a certain shortening value until the end), and (4) initially layer-perpendicular passive marker lines. In the matrix at the outer arc of the fold, all strain measures result in similar divergent fan patterns. Therefore, divergent foliation fans around natural folds cannot readily be associated with the finite strain orientation as they may reflect other strain measures. In the simulated folds, the convergent fans in the stronger layer show differences between the different strain measures, which are associated with a 90°-switch of the major principal strain from a layer-perpendicular to a layer-parallel orientation at the outer arc. A similar observation is made in one of three studied natural folds (near Ribadeo and Luarca, NW Spain). It is suggested that the convergent foliation fan pattern inside a fold is better suited for strain estimates than the divergent fan around a fold.

Rock deformation and foliation development are two intimately coupled processes. For example, the axial plane foliation in folded rocks has a very characteristic geometrical relationship to the folds, which can be used by field geologists to determine the geometry of unexposed parts of folds. Commonly, the foliation is refracted across boundaries between lithologies of different competence. The refraction angle has been related through analytical expressions to the viscosity ratio between the two lithologies (Treagus 1983, 1988, 1999; Talbot 1999; Mulchrone & Meere 2007), very similar to the refraction of optical light. Treagus & Sokoutis (1992) performed laboratory experiments in viscous materials to test the previously derived analytical expressions in simple-shear deformation. The findings of these studies have been applied, for example, to infer the relative strengths of metamorphic rocks in the Appalachians (Groome & Johnson 2006). To relate the analytical expressions and the laboratory experiments to the natural foliation refraction, all of these studies assume that the foliation orientation reflects the major principal finite strain orientation. This assumption stands since the early days of structural geology (Sharpe 1847; Sorby 1853; Haughton 1856; Cloos 1947; Ramsay 1967, pp. 180–182; Siddans 1972; Wood 1973, 1974; Tullis & Wood 1975; Price & Cosgrove 1990, pp. 450–453; Twiss & Moores 2007, pp.

400–405 & pp. 426–427), but it is, however, far from a proven fact.

For example, if the foliation develops late during the deformation history, it rather represents a cumulative strain (from onset of foliation development until the end of deformation) than the finite strain. Wood & Oertel (1980) compared the orientation of slaty cleavage with that of ellipsoidal strain markers in the Cambrian Slate Belt of Wales, assuming that the latter orientation represents the finite strain. They found a relationship but not an exact match between the two, suggesting that the cleavage is influenced by, but does not exactly follow, the orientation of the major principal finite strain. Oertel *et al.* (1989) compared the orientation of two different strain markers on the Appalachian Plateau, that is, the foliation orientation with the orientation of deformed crinoid columnals, in which the latter is assumed to represent the finite strain. Again, a relationship but not an exact match is found between the two. A review of the use and limitations of foliation orientation as an indicator for finite strain orientation is given by Oertel (1983).

If foliation refraction occurs around folded layers, more complex foliation refraction patterns can occur: the foliation fans (Ramsay 1967, pp. 403–405; Ramsay & Huber 1987, pp. 463–472). Two different types may occur: convergent and divergent foliation fans. The former occurs if the

foliation from the two limbs intersects in the inner arc of the fold; the latter occurs if the foliation from the two limbs intersects in the outer arc of the fold. Mechanically stronger layers tend to exhibit convergent fans while mechanically weaker layers tend to exhibit divergent fans. Such foliation fan patterns around folds are quite common features in outcrop-scale folds (e.g. Viola & Mancktelow 2005), but also occur on a smaller scale in thin sections (e.g. Aerden *et al.* 2010). Debacker *et al.* (2006) used foliation fan patterns to distinguish between folds amplifying prior to foliation development and folds amplifying contemporaneously with foliation development. Finally, Viola & Mancktelow (2005) demonstrated that foliation fans can even be folded themselves if the fold amplification is large enough.

Recently, Adamuszek *et al.* (2013) developed the Large Amplitude Folding theory, an analytical model to accurately calculate the geometry of high-amplitude folds. An extensive review of the information that may be gleaned from fold shapes can be found in Hudleston & Treagus (2010). However, there is no analytical method to calculate the strain inside and around a fold of large amplitude. A possible way to assess not only the finite strain orientation, but also the orientation of other strain measures is by conducting numerical experiments of buckle folding. Numerical methods allow for a direct calculation, visualization, and quantification of various strain measures inside and around a fold. Early finite-element (FE) simulations (Dieterich 1969; Dieterich & Carter 1969; Shimamoto & Hara 1976) calculated and visualized the orientation of the principal finite strain and of the principal stress to investigate the transition from inner-arc shortening to outer-arc extension in single-layer folds. The same phenomenon was investigated by Hudleston & Lan (1993), Hudleston & Lan (1995), and Lan & Hudleston (1995) by calculating the aspect ratios of the finite strain ellipses exactly on the fold axial plane (FAP) from their FE calculations. Recent studies that made extensive use of stress and strain orientation calculations in numerical FE simulations include Viola & Mancktelow (2005) studying foliation fans around folds, Frehner & Schmalholz (2006) studying the development of asymmetrical parasitic folds in multilayer systems, Reber *et al.* (2010) focusing on the stress orientation rotation on the limbs of amplifying folds and induced fracturing, and Frehner (2011) investigating the dynamic migration of the neutral lines through a single layer. All these studies use the finite strain, the infinitesimal strain, or the stress orientations. In contrast, the orientation and refraction patterns of foliation, which form during an arbitrary stage during folding, have not been investigated to date, and are the main subject of this study.

This study presents FE simulations of single-layer buckle folds for which various strain measures are calculated, including not only the finite strain and the infinitesimal strain, but also intermediate strain measures. The orientations of all of these strain measures inside the fold and in the surrounding matrix are visualized and quantified to describe the refraction pattern. These strain refraction patterns are compared to foliation refraction patterns in and around natural outcrop-scale folds in NW Spain.

## Numerical method and model setup

For numerically simulating viscous buckle folding the FE method (e.g. Cuvelier *et al.* 1986; Hughes 2000; Zienkiewicz & Taylor 2000) is employed. The self-developed numerical code is implemented in MATLAB and simulates the two-dimensional (2D) incompressible plane-strain deformation of either linear (Newtonian) or power-law viscous isotropic materials in the absence of gravity. A detailed description of the numerical implementation is given in Frehner & Schmalholz (2006), Frehner (2011) and references therein. The code has successfully been benchmarked against the analytical fold growth-rate solution of both Fletcher (1977) for Newtonian rheology, and of Fletcher (1974) for power-law viscous rheology. Recent studies that also made use of this code investigated the development of asymmetrical parasitic folds in multilayers (Frehner & Schmalholz 2006), the dynamic behaviour of the neutral lines in amplifying single-layer folds (Frehner 2011), and the feasibility of dynamically unfolding mountain-scale folded cross-sections (Frehner *et al.* 2012).

In this study, upright symmetrical single-layer folds with dominant initial wavelength under horizontal shortening are studied. Out of all possible wavelengths, the dominant wavelength is the one with the highest initial growth rate and is therefore strongly related to the wavelength occurring in natural folds (Adamuszek *et al.* 2013). Both the folding layer and the surrounding matrix are isotropic and homogeneous. The initial setup for all simulations (Frehner 2011, fig. 3) comprises a rectangular box containing a horizontal layer embedded in a matrix of lower viscosity. The perfectly welded upper and lower layer interfaces exhibit a sinusoidal initial perturbation of dominant wavelength (Fletcher 1974, 1977) with an amplitude-to-layer thickness ratio of 0.01. The applied boundary conditions are: zero traction and zero boundary-perpendicular velocity (immobile free slip wall) at the lower and left boundaries; zero traction (free surface) at the top boundary; and zero traction with a prescribed horizontal velocity (moving free

slip wall) at the right boundary. The prescribed horizontal velocity is adjusted during the simulations to maintain a constant background shortening strain rate. Both the upper and lower boundaries are set outside the zone of contact strain (Ramsay & Huber 1987, pp. 352–363) to avoid boundary effects.

Each time step of a FE simulation provides the velocity gradient tensor,  $\dot{\mathbf{H}}$  with components  $\dot{H}_{ij} = \partial v_i / \partial x_j$ , at every integration point of the numerical domain in the Cartesian  $(x_1, x_2)$ -coordinate system, where  $v$  is velocity and  $x$  is the coordinate direction. The infinitesimal deformation gradient tensor at a given time step,  $m$ , is calculated as

$$\mathbf{D}_m = [\mathbf{I} + \Delta t \dot{\mathbf{H}}_m] \quad (1)$$

where  $\mathbf{I}$  is the  $2 \times 2$  identity matrix, and  $\Delta t$  is the time increment. The infinitesimal deformation gradient tensor describes the deformation over one time increment. If the time increment chosen is small enough, it represents the instantaneous deformation. The finite deformation gradient tensor,  $\mathbf{F}_m$  (Haupt 2002), at a given time step,  $m$ , is calculated using the Euler integration method as

$$\mathbf{F}_m = \prod_{k=1}^m \mathbf{D}_k \quad (2)$$

where  $\prod$  denotes the product. The finite deformation gradient tensor describes the entire deformation path from the beginning of the simulation ( $k = 1$ ) to the current time step. Equation (2) can be modified to calculate the incremental deformation gradient tensor:

$$\mathbf{C}_{n-m} = \prod_{k=n}^m \mathbf{D}_k, \quad n < m. \quad (3)$$

The incremental deformation gradient tensor records only the deformation path from an intermediate time step ( $k = n$ ) to the current time step and is therefore an intermediate strain measure between the infinitesimal and finite strain. All three strain measures can be used to calculate a left Cauchy-Green tensor (Haupt 2002):

$$\begin{aligned} \mathbf{B}_m^D &= \mathbf{D}_m \mathbf{D}_m^T, & \mathbf{B}_{n-m}^C &= \mathbf{C}_{n-m} \mathbf{C}_{n-m}^T, \\ \mathbf{B}_m^F &= \mathbf{F}_m \mathbf{F}_m^T. \end{aligned} \quad (4)$$

The eigenvectors and the square roots of the eigenvalues of these three left Cauchy-Green tensors correspond to the orientation and magnitudes of the infinitesimal ( $\mathbf{B}_m^D$ ), incremental ( $\mathbf{B}_{n-m}^C$ ), and finite ( $\mathbf{B}_m^F$ ) strain ellipse axes (Frehner 2011) at a given time step  $m$ . The orientation of the long strain ellipse axes (major principal strains) will now be

visualized and quantified for various numerical simulations.

## Numerical results

Figure 1 shows three subsequent shortening stages (top to bottom) of a single-layer folding simulation with a viscosity ratio of  $R = 100$  between the folding layer and the surrounding matrix. For each stage the orientation and magnitude of the major principal strain is plotted as short lines for the three strain measures infinitesimal (left, Fig. 1a, e & j), incremental (centre), and finite strain (second from right, Fig. 1c, h & n). In addition, the orientation of initially vertical passive marker lines is plotted on the right-hand side (Fig. 1d, i & o). Naturally, the strain ellipses and their long axes are more elongated when more strain is recorded, which leads to a denser pattern for higher shortening values (top to bottom in Fig. 1) and for measures recording more strain (left to right in Fig. 1). Also, the lower-viscosity matrix experiences higher strain compared to the folding layer, which experiences more rotation. However, in the following the focus is on the orientation patterns of the major principal strains and not on their magnitudes.

### *Divergent fan pattern in the matrix*

The major principal strain for all strain measures exhibits a very distinct divergent fan in the matrix at the outer arc of the fold close to the hinge. In many cases, these divergent fans even show horizontal orientations close to the layer interface. For a given shortening value (one row in Fig. 1), the patterns of the divergent fans are very similar for the infinitesimal and different incremental strain measures (e.g. Fig. 1a, b), but somewhat different for the finite strain (e.g. Fig. 1c). This may indicate that the divergent fan pattern is influenced by the pure-shear shortening prior to buckling initiation, which is recorded by the finite strain but not by the other strain measures. At low shortening values (Fig. 1a–c) the divergent fans occupy a large area around the fold. For increasing shortening values (Fig. 1j–n) the divergent fans are more restricted to the vicinity of the fold while further away the major principal strains are sub-parallel to the FAP and do not exhibit a fan. The orientation of the passive marker lines (Fig. 1d, i & o) hardly exhibits a convergent fan pattern in the matrix at the outer arc of the fold. If anything, the divergent fan weakly resembles the pattern of the finite strain. The fan patterns in the matrix at the inner arc of the fold are much less pronounced. At low shortening values ( $s = 21.4\%$ , Fig. 1a–c), a very slight divergent fan develops while at higher shortening

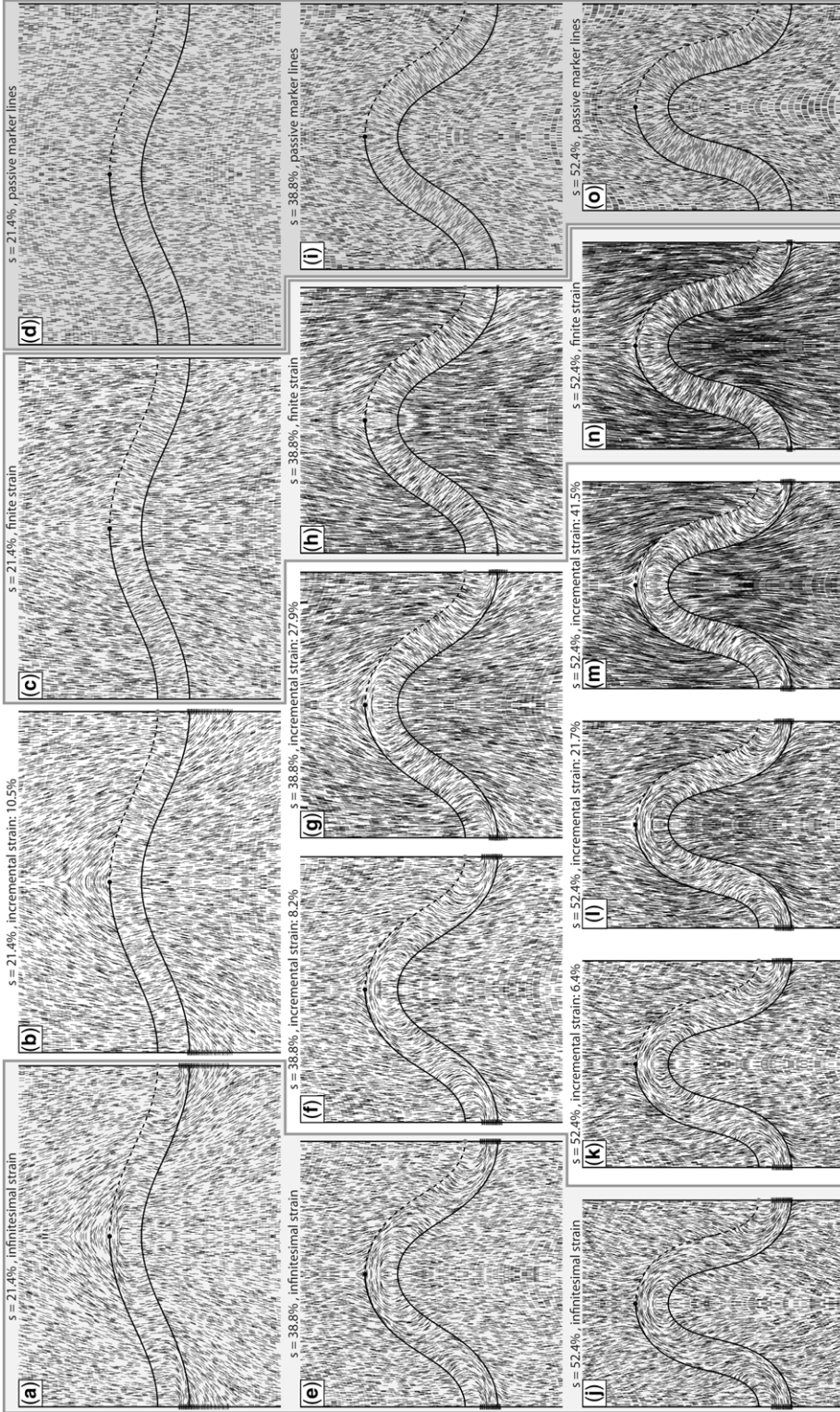


**Fig. 1.** Snapshots of a finite-element simulation of a single-layer buckle fold with a viscosity ratio of  $R = 100$  between the folding layer and the surrounding matrix. Top to bottom represents increasing shortening, that is,  $s = 21.4\%$ ,  $38.8\%$ , and  $52.4\%$ . Lines represent the orientation and magnitude (indicated by line length) of the major principal strain for the infinitesimal, finite, and incremental strain measures in snapshots on the left-hand side (a, e, j), in the second snapshots from the right (c, h, n), and the snapshots in-between (b, f, g, k, l, m), respectively. The amount of strain recorded by the incremental strain measure (equation (3)) is indicated above the respective snapshots. The snapshots on the right-hand side (d, i, o) show the orientation of initially vertical passive marker lines. The dashed fold interface connecting the antiform (black dot) with the synform (grey dot) is used in later figures.

values (Fig. 1e–h) a convergent fan develops that becomes more pronounced with increasing shortening (Fig. 1j–n).

### *Convergent fan pattern in the folding layer*

The major principal strain for all strain measures exhibits a convergent fan at the inner arc of the higher-viscosity folding layer. Towards the outer arc of the layer the strain orientations are strongly modified and for most strain measures and shortening values the strain orientations switch from a convergent fan to a divergent fan pattern at the outer arc of the fold. This switch of strain orientation appears closer to the inner arc of the layer for strain measures recording smaller amounts of strain (e.g. infinitesimal compared to finite strain, Fig. 1j compared to Fig. 1n) and for higher shortening values (e.g. Fig. 1j compared to Fig. 1a). The switch from a convergent fan at the inner arc to a divergent fan at the outer arc can be associated with the migration of the neutral line from the outer towards the inner arc with increasing shortening (Frehner 2011). For the two end-member cases of either finite or infinitesimal strains the same switch of strain orientation was also observed by Dieterich (1969), Dieterich & Carter (1969), and Viola & Mancktelow (2005). The only case in Figure 1 where no such switch appears is for finite strain at a shortening of 21.4% (Fig. 1c). As a result of the switch of strain orientation in the hinge area, the major principal strain orientation patterns are somewhat, but not substantially, different for the different strain measures. The passive marker line orientation pattern in the folding layer (Fig. 1d, i & o) exhibits a convergent fan throughout the entire folding process and no switch of orientation to a divergent fan ever occurs. However, the convergent fan of the passive marker lines (Fig. 1d, i & o) resembles the part of the major principal finite strain orientation pattern (Fig. 1c, h & n) at the inner arc of the fold, where the latter is convergent.

### *Strain orientation quantification*

For the simulation shown in Figure 1 the orientation of the fold interface and the major principal strains is plotted in Figure 2 in the same way as depicted in the figures for the natural folds (see ‘Natural examples’). All orientations are measured from the black to the grey dot along the outer arc of the antiform exactly at the fold interface (dashed line in Fig. 1). Because the numerical folds are upright and symmetrical, the angle to the FAP (vertical axis in Fig. 2a, both axes in Fig. 2b) can be read as (i) limb dip for the fold interface data and (ii) deviation from vertical for the strain orientation data, respectively. Also, all FE simulations are 2D

and therefore only line orientations and not plane orientations can be calculated. However, to be consistent with the figures with the natural fold data, which are oriented in the 3D space, the term ‘Dihedral angle’ is used for the axis labels in Figure 2.

The strain orientations in the matrix are remarkably similar for all shortening values and for all strain measures. An exception is the finite strain at a shortening of 21.4% (Fig. 2a, b). In all other cases the major principal strains are perpendicular ( $-90^\circ$ ) to the FAP at the antiform hinge. Along the outer arc of the fold this value increases resulting in divergent fan patterns around the antiform (Fig. 1). At a shortening of 21.4% (Fig. 2a, b) the angles between the major principal strains in the matrix and the FAP are always negative and the divergent fans cover the entire fold from antiform to synform. Hence, the major principal strains also form a divergent fan in the inner arc of the adjacent synform (close to the grey dot in Fig. 1). In the higher shortening cases (Fig. 2c–f) the angles between the major principal strains in the matrix and the FAP become positive close to the adjacent synform indicating a convergent fan at the inner arc of the fold. However, these inner-arc convergent fans are much less pronounced than the outer-arc divergent fans. The transition from convergent to divergent fan (zero crossing) is on the antiform-side from the inflection point for all strain measures and closer to the antiform for strain measures recording smaller amounts of strain. The exceptional case of finite strain at a shortening of 21.4% (Fig. 2a, b) shows a negligible convergent fan at the inner arc of the synform and a divergent fan at the outer arc of the antiform, but without a switch of the major principal strain to  $-90^\circ$ . In this case the transition from convergent to divergent fan is slightly on the synform-side from the inflection point. The passive marker lines in the matrix roughly follow the finite strain orientation, in particular close to the synform and for large shortening values. The passive markers do not rotate close to the fold hinge due to the traction-free boundary conditions and their orientation strongly deviates from that of the finite strain close to the antiform hinge. In the case of 21.4% shortening (Fig. 2a, b) the passive marker line orientation exhibits a convergent fan along the entire fold and resembles the major principal finite strain orientation only very weakly.

The strain orientations in the higher-viscosity folding layer (dashed lines in Fig. 2) share some common features for the different strain measures and for the different shortening values. With the exception of finite strain at 21.4% shortening, all major principal strains at the antiform hinge are perpendicular ( $-90^\circ$ ) to the FAP and parallel to the fold interface, which is represented by a  $90^\circ$  difference between the strain orientations and the

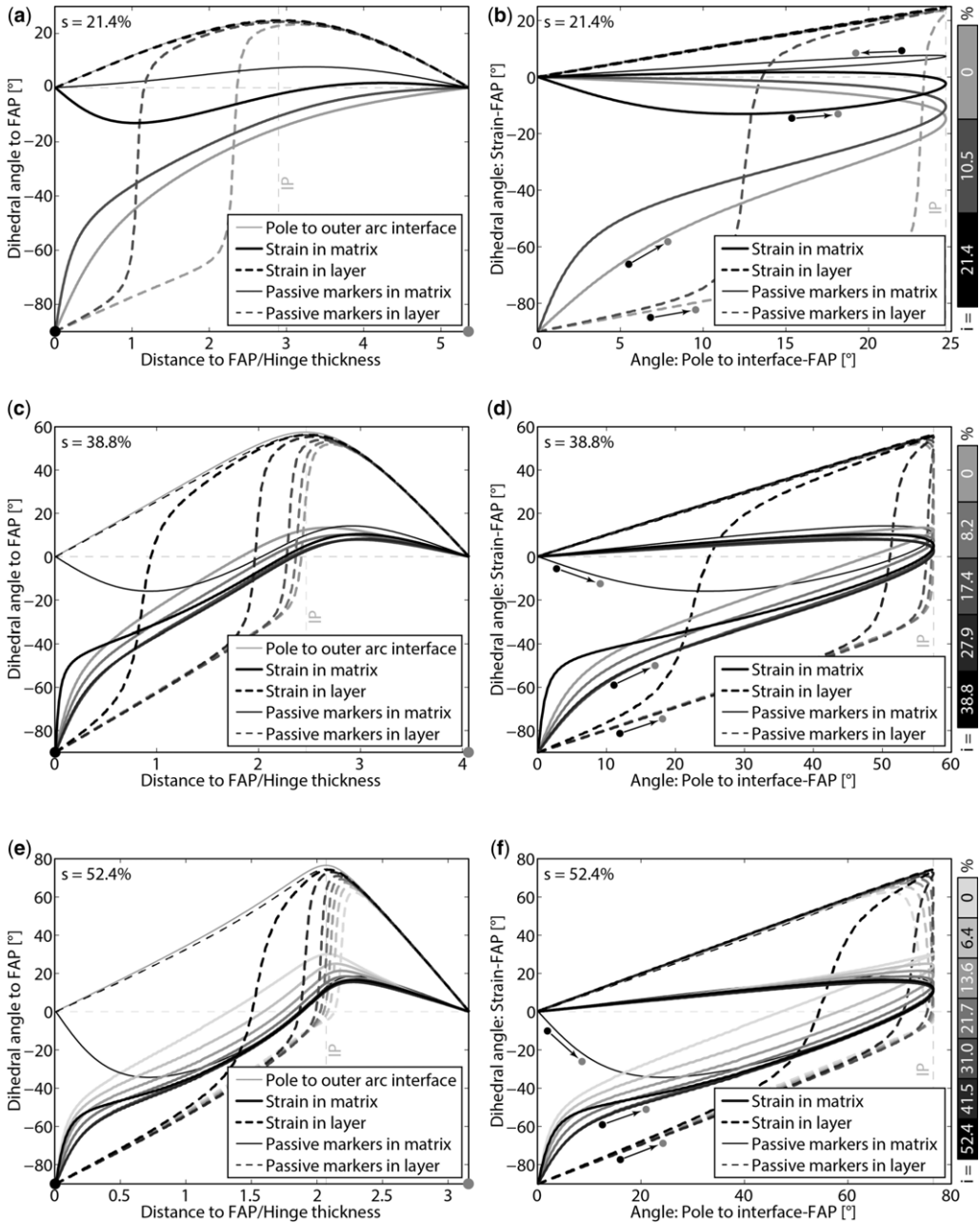


**Fig. 2.** Strain and fold interface orientation data for the same finite-element simulation as in Figure 1 (viscosity ratio  $R = 100$ ) for the same three shortening values,  $s$ , as in Figure 1 (top to bottom). The data are taken from the outer arc of the fold along the dashed line from the black to the grey dot in Figure 1 (also indicated in (a), (c) and (e)). Different line grey levels represent different strain measures, whereas black represents finite strain, lightest grey infinitesimal strain, and intermediate grey levels different incremental strains, as indicated in the grey level-bar. Positive values for strain orientation indicate a convergent fan; negative values indicate a divergent fan. IP, inflection point. (a, c, e) Angle between major principal strains and the fold axial plane (FAP) plotted v. the normalized distance from the FAP. For the fold interface, the angle between the pole to the interface and the FAP is plotted. (b, d, f) Angle between major principal strains and the FAP plotted v. the angle between the pole to the fold interface and the FAP. Small arrows indicate the direction from the antiform towards the synform (black towards grey dot in Fig. 1).

fold interface in Figure 2a, c, and e. Along the fold, the major principal strains maintain their sub-parallel orientation to the fold interface before they switch to a layer-perpendicular orientation indicated by negligible difference between the strain orientations and the fold interface close to the synform. The  $90^\circ$ -switch from a layer-parallel to a layer-perpendicular strain orientation happens within a very short distance on the antiformal side from the inflection point and closer to the antiformal for strain measures recording larger amounts of strain. At higher shortening (Fig. 2e) and for strain measures recording small amounts of strain the  $90^\circ$ -switch happens slightly on the synform-side from the inflection point. This  $90^\circ$ -switch of strain orientation can also be identified in Figure 2b, d, and f, where the major principal strain orientations plot with a slope of about one for a large part of the fold, which indicates either layer-parallel or layer-perpendicular orientations. The finite strain at 21.4% shortening (Fig. 2a, b) maintains a layer-perpendicular orientation along the entire fold. The

same is true for the passive marker lines in the folding layer (also Fig. 1d, i & o).

### Varying viscosity ratios

FE simulations were also performed for viscosity ratios ( $R$ ) of 25 and 40 between the folding layer and the surrounding matrix. For a shortening of 38.8% the fold interface, strain, and passive marker line orientation data are plotted in Figure 3 and some simulation snapshots are shown in Figure 4. The strain orientations in the matrix along the fold interface for a small viscosity ratio of  $R = 25$  (solid lines in Fig. 3a, b) are different for the different strain measures, while the different strain measures are comparable for higher viscosity ratios, particularly on the synform-side from the inflection point ( $R = 40$  and  $R = 100$ ; Figs 3c, d & 2c, d). However, the absolute values of the dihedral angles are generally smaller for lower viscosity ratios, meaning that the fan patterns are less pronounced. At a viscosity ratio of 25 (Fig. 3a, b), the

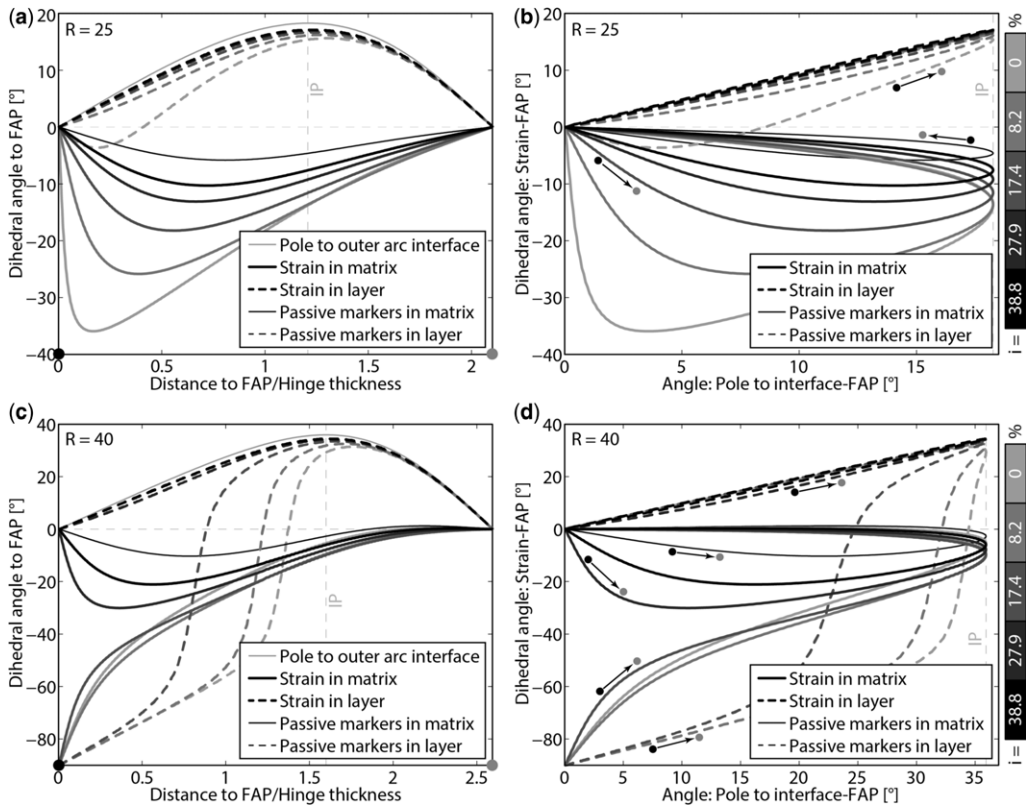


**Fig. 3.** Strain and fold interface orientation data for two finite-element simulations with viscosity ratio  $R = 25$  (upper) and 40 (lower) for a shortening of  $s = 38.8\%$ . The left (a, c) and right (b, d) representations of the data are the same as in Figure 2.

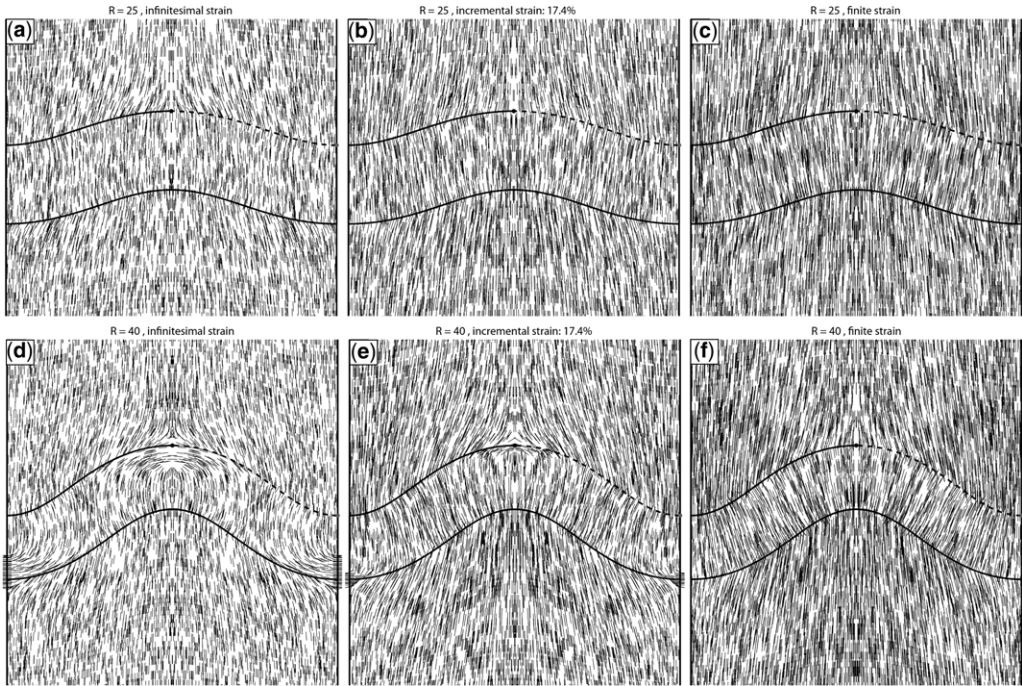


**Fig. 4.** Snapshots of two finite-element simulations of a single-layer buckle fold with viscosity ratios of  $R = 25$  (top, **a–c**) and 40 (bottom, **d–f**) for a shortening of  $s = 38.8\%$ . Lines represent the orientation and magnitude (indicated by line length) of the major principal strain for the infinitesimal, incremental, and finite strain measures in snapshots on the left-hand side (**a** and **d**), in the centre (**b** and **e**), and on the right-hand side (**c** and **f**), respectively. The amount of strain recorded by the incremental strain measure (equation (3)) is 17.4%.

major principal strains in the matrix exhibit divergent fan patterns along the entire fold. For increasing viscosity ratios ( $R = 40$  and  $R = 100$ ; Fig. 2c, d) an increasing portion of the matrix at the inner arc of the synform exhibits convergent fans and Figure 3c and d mark about the transition, where the major principal strains are parallel to the FAP in the matrix at the inner arc of the synform (also Fig. 4d–f). For a low viscosity ratio of  $R = 25$  the major principal strains do not switch to a layer-parallel orientation at the antiform hinge ( $0^\circ$  dihedral angle at the antiform in Fig. 3a, b; also Fig. 4a, b); for the intermediate viscosity ratio of  $R = 40$  only the strain measures recording a small amount of strain show such a switch (Figs 3c, d & 4d–f); and for a high viscosity ratio ( $R = 100$ ) all strain measures show this switch (Figs 2b, c & 1e–h).

In the folding layer with higher viscosity the strain orientations are very similar for all strain measures in the case of a viscosity ratio of 25 (Fig. 3a, b). The major principal strain orientations are close to layer-perpendicular and exhibit convergent fans along the entire fold. Only the infinitesimal strain measure shows a slight divergent fan in a very restricted area around the hinge,

but exactly at the hinge the major principal infinitesimal strain returns to a parallel orientation to the FAP and does not show the  $90^\circ$ -switch as is the case for higher viscosity ratios (Figs 3c, d & 2c, d). The resulting convergent fan is negligible and not even detectable in Figure 4a. For an intermediate viscosity ratio of 40 the finite strain and the incremental strain measure recording the most strain maintain a layer-perpendicular orientation along the entire fold. The strain measures recording a smaller amount of strain switch by  $90^\circ$  to a layer-parallel orientation on the antiform-side from the inflection point. For a high viscosity ratio of 100 all strain measures show this  $90^\circ$ -switch (Fig. 1e–h).

#### *Power-law viscous rheology*

Various numerical FE simulations were performed using power-law viscous rheology with various combinations of the power-law exponent of the folding layer and the surrounding matrix. Generally, the observations made above for the Newtonian cases do not change for the power-law viscous cases. For example, Figure 5 shows the major principal strain orientations plotted against

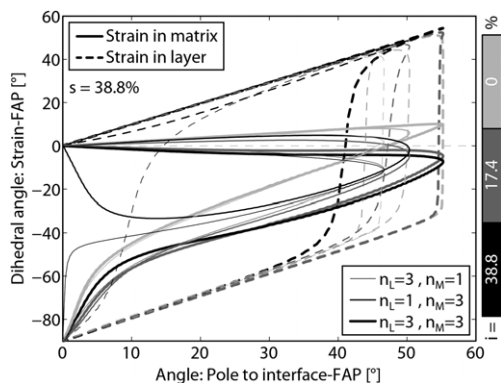


**Fig. 5.** Angle between major principal strains and the fold axial plane (FAP) plotted v. the angle between the pole to the fold interface and the FAP at a shortening of  $s = 38.8\%$  for three different power-law viscous FE simulations with a reference viscosity ratio of  $R = 40$  and a combination of power-law exponents of the layer ( $n_L$ ) and the matrix ( $n_M$ ) of  $n_L = 3, n_M = 1$  (thin lines),  $n_L = 1, n_M = 3$  (intermediate lines), and  $n_L = 3, n_M = 3$  (thick lines). Different line grey levels represent different strain measures, whereas black represents finite strain, intermediate grey incremental strain, and lightest grey infinitesimal strain. The amount of strain recorded by the incremental strain measure (equation (3)) is  $17.4\%$ .

the fold interface orientations for FE simulations using a power-law exponent of 3 for the layer and/or the matrix, a reference viscosity ratio of 40, and a shortening of 38.8%. Three strain measures for each simulation are shown in Figure 5: infinitesimal, finite, and incremental strain, the latter recording the last 17.4% shortening. The different power-law viscous rheologies lead to different amplification rates of the dominant wavelength (Fletcher 1974) and therefore to different maximum limb dips at the same shortening value. Apart from this, the strain orientation patterns are similar for all power-law viscous cases and similar to the Newtonian case (Fig. 3d). These similarities include: (i) a  $90^\circ$ -switch of the major principal strains in the folding layer from a layer-perpendicular orientation close to the synform to a layer-parallel orientation close to the antiform, whereas this switch happens on the antiform-side from the inflection point and (ii) a smooth transition of the major principal strain orientations in the matrix from a divergent fan close to the antiform hinge to a weak or negligible convergent fan at the inner arc of the adjacent synform.

## Natural examples

In the following section, the aim of analysing the foliation orientation in natural folds is not a

quantitative one-to-one comparison between natural and numerical folds, but a qualitative one. The geometry of the selected natural fold examples is much more complex than the relatively simple symmetrical single-layer folds of the performed numerical study. Nevertheless, a qualitative comparison allows foliation-orientation features to be identified that can be reproduced by the numerical simulations. For a one-to-one reproduction of the natural fold geometries and the corresponding foliation orientations, inverse numerical methods may be applied (e.g. Lechmann *et al.* 2010; Frehner *et al.* 2012). However, for accurate modelling results using such methods, various physical parameters during fold formation have to be known quite precisely, such as pressure, temperature, or the rheological flow-law.

For the qualitative comparison of the numerical results with natural examples, three outcrop-scale folds with well-developed foliation refraction patterns were selected. The studied outcrops are located in the Western Asturian–Leonese Zone (WALZ) of the Variscan belt in NW Spain (Marcos 1973; Bastida & Pulgar 1978; Laner 2010; inset in Fig. 6). The WALZ comprises metasedimentary rocks of lower Palaeozoic age, unconformably overlying Precambrian turbidites (Bastida *et al.* 1986). The entire zone was affected by Variscan nappe stacking with top-to-the-east thrusting and co-eval folding of both the sedimentary cover and the underlying basement units. Although three deformation phases have been distinguished, the fold axes for these events are generally aligned parallel (Fernández *et al.* 2007, and references therein).

Folds at two sites on the Cantabrian coast were investigated in this study. Two fold examples have been selected from a site at Portizuelo, east of Lluarca, Asturias; a third example is from a site at Benquerencia, west of the town of Ribadeo, Galicia. At Portizuelo, Lower Ordovician rocks are summarized as Lluarca Slates, comprising quartzites, sandstones, and slates deposited in an extensional regime on a passive continental margin (Marcos 1973). The abundant intercalations of layers of different strength are deformed into upright to slightly east-verging folds with wavelengths of up to several tens of metres (related to D3 folding according to Bastida *et al.* 1986). At Benquerencia, Cambrian metasediments of the Cándana Group are deformed into recumbent folds in the normal limb of the Foz-Tapia Anticline, a major fold of the Mondoñedo nappe (Bastida *et al.* 1986). Folds of several hundred metres amplitude and accompanying asymmetrical second-order folds of several metres in size can be identified in the intercalated sandstones and shales, which deformed under greenschist facies metamorphic conditions (Fernández *et al.* 2007).

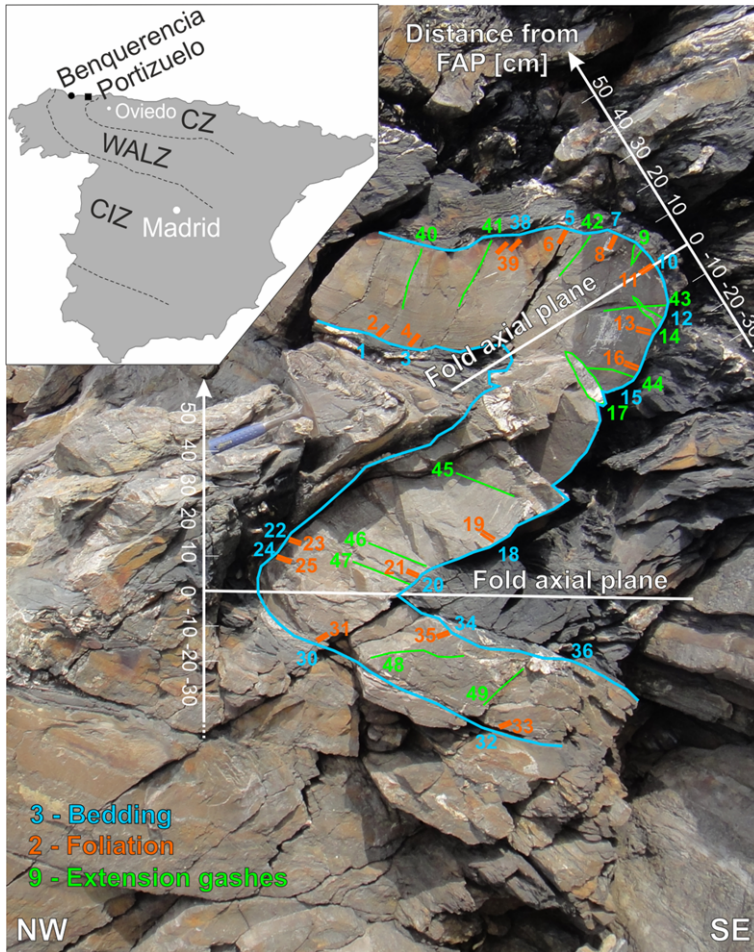


**Fig. 6.** Outcrop picture of a SE-verging synform/antiform fold train at Portizuelo, NW Spain. Orientations of bedding, foliation and extension gashes were measured at the positions indicated by numbers exclusively within the sandstone layer. The fold axial planes (FAP) of the upper and lower fold are not parallel and both are used in Figure 7. Inset in the upper-left corner shows the location of both investigated sites and their positions in the Hercynian orogenic units (CZ, Cantabrian Zone; WALZ, Western Asturian–Leonese Zone; CIZ, Central Iberian Zone) of the Iberian Peninsula (modified after Bastida *et al.* 1986).

### *Outcrop example 1 (Portizuelo)*

The first outcrop example is located at the Portizuelo site ( $43^{\circ}32'56''\text{N}$ ,  $6^{\circ}30'36''\text{W}$ ). A sandstone layer is folded into a SE-vergent synform/antiform train, embedded in an indistinct shale matrix (Fig. 6). In addition to the axial plane foliation, numerous extension gashes overprinting the sedimentary bedding in the sandstone layer were measured. Some broader extension gashes are clearly related to outer-arc extension (e.g. measurement numbers 9, 14, 17 in Fig. 6). In contrast, the more abundant thinner veins (measurement

numbers 40–49 in Fig. 6) are not restricted to the outer-fold arcs, but are cross-cut by the broader veins. They may reflect an earlier deformation stage, possibly related to burial of the sediments, or movement and opening along an early refracted foliation surface (Ramsay 1967). The two folds shown in Figure 6 have two non-parallel FAPs (upper and lower). Therefore, both FAPs are considered in Figure 7, where the relationships between bedding, foliation, and extension gashes are plotted against the distance to the FAPs (Fig. 7a) and the orientation of the FAPs (Fig. 7a, b).

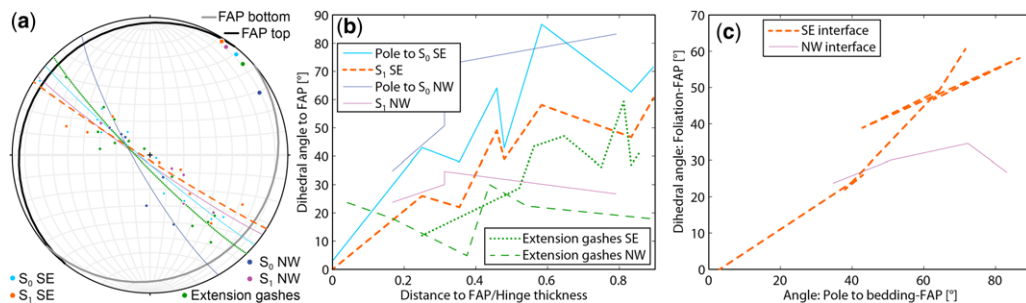


**Fig. 7.** Field measurements of the outcrop shown in Figure 6. **(a)** Lower-hemisphere equal area projection. Small dots represent poles to plane measurements. Coloured lines and large dots represent the best fitting great circle with its pole to the data of the same colour. FAP bottom and FAP top denote the fold axial plane of the bottom and top fold in Figure 6; S<sub>0</sub> SE and S<sub>1</sub> SE denote the bedding and foliation at the southeastern fold interface (right blue line in Fig. 6); S<sub>0</sub> NW and S<sub>1</sub> NW denote the bedding and foliation at the northwestern fold interface (left blue line in Fig. 6). **(b)** Dihedral angle between plane measurements and the FAP plotted v. the normalized distance of the measurements from the FAP. Measurements at the southeastern fold interface are plotted with respect to the upper FAP; measurements at the northwestern fold interface are plotted with respect to the lower FAP. Positive values for foliation (S<sub>1</sub>) indicate a convergent foliation fan; negative values indicate a divergent fan. For the bedding (S<sub>0</sub>), the angle between the pole to the bedding and the FAP is plotted instead of the dihedral angle. **(c)** Dihedral angle between the foliation and the FAP plotted v. the angle between the pole to the bedding and the FAP. In (b) and (c) measurements 9, 14, and 17 (Fig. 6) are omitted because they exhibit a different orientation trend from the other extension gashes.

### Outcrop example 2 (Portizuelo)

The second studied fold crops out close to the first one at Portizuelo (43°32′49″N, 6°30′45″W). Several sandstone layers are folded into an upright, slightly SE-verging synform (Fig. 8). Although a low viscosity matrix is not exposed at this location, the sandstone layers show varying orientation of axial plane foliation in this fold. The more tightly folded inner sandstone layer (above the blue line in Fig. 8) shows a narrow convergent foliation fan (measurement points 19–24 in Fig. 8). Below the blue line, the outer sandstone layer exhibits a more widely spaced convergent foliation fan (measurement points 2, 4, 6, . . . , 18 in Fig. 8). Both of these foliation fans indicate a layer-parallel shortening direction. In addition, layer-perpendicular shortening structures can be identified close to the fold hinge at the outer arc of the outer layer. A quartz-filled extension vein is folded in layer-perpendicular direction and intersected and deformed by layer-parallel pressure-solution surfaces (inset in Fig. 8). At the outer arc of the fold these pressure-solution surfaces can be identified in the field but are hardly abundant enough to form a bedding-parallel foliation. Similar to Figure 7, the relation between the structural elements and their position along the fold is shown in Figure 9.

### Outcrop example 3 (Benquerencia)

At the Benquerencia site, a third fold was examined for this study (43°34′6″N, 7°12′49″W, Fig. 10),

which formed at slightly higher metamorphic conditions compared to the first site, as indicated by the higher intensity of axial plane foliation. The relation between the structural elements and their position along the fold are shown in Figure 11. The angles between the foliation in the quartzite and in the shale measured at the identical position around the fold are rather small (Fig. 11), which suggests that the viscosity ratio between the layers is smaller during deformation compared to the first site.

## Discussion

In this study, various strain measures (finite, incremental, and infinitesimal strain, and passive marker lines) are considered, which may represent the onset of foliation development at different stages during deformation. If so, finite strain would represent an early foliation in the folding history, which continues to be modified by the changing stress state during folding. Initially vertical passive marker lines represent a foliation development prior to buckling initiation, which is not modified any more during folding and only rotates passively. A foliation developing at a given time during folding does not record the early pure-shear shortening and thickening of the layer prior to buckling initiation and is represented by the incremental strain. In contrast, infinitesimal strain represents a foliation development during the very last stage of folding. Brittle fractures, for example, may develop during this stage.

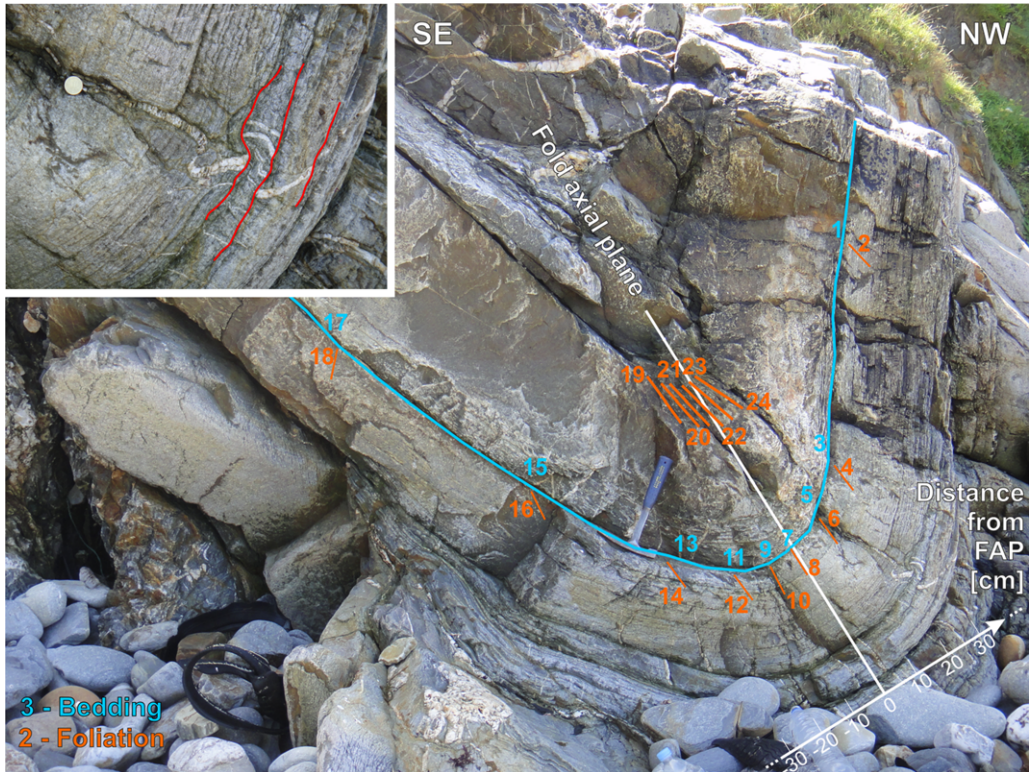


**Fig. 8.** Upright, slightly SE-verging synform at Portuzuelo developed in sandstone beds. Bedding and foliation were measured at the indicated positions. Inset: Zoom of one extension gash in the outermost sandstone layer slightly NW of the fold axial plane (FAP), which is folded in layer-perpendicular direction and partially truncated by layer-parallel pressure-solution surfaces. Traced in red are the few pressure-solution surfaces that can be identified as such in the field, but there may be more such surfaces that are not traced here.

In both numerical and natural folds the strain pattern depends on the geometry and amplitude of the initial perturbation on the layer interfaces (Mancktelow 2001). For example, a layer with large initial perturbation amplifies earlier than one with small initial perturbation and experiences less pure-shear shortening prior to buckling initiation. Therefore, the initial perturbation also influences the orientation pattern of the strain measures recording this early deformation stage (i.e. finite strain and incremental strain recording a large amount of strain).

In the following, the geometrical relationships for the various scenarios of foliation development inferred from the strain measure orientation patterns are discussed and qualitatively compared to the field observations. It is emphasized that a quantitative one-to-one comparison is not feasible because the numerical simulations do not cover all the natural complexities, such as multilayer folding (Fig. 8), non-parallel FAPs in adjacent folds (Fig. 6), or strong anisotropy (Fig. 10).

#### *Comparison between numerical and natural folds*

The data curves for the natural data are not as smooth as for the numerical data due to measurement inaccuracies and natural variations. In addition, measurements made on both sides of the FAP of a natural fold are combined in the data plots. If the folds are not perfectly symmetrical with respect to the FAP, this introduces some data variability. Nevertheless, some common features between natural and numerical data can still be recognized. For example, the foliation in the weaker shale around the fold in Figure 10 exhibits a clear divergent fan (negative values in Fig. 11b, c). With increasing distance from the FAP the absolute value of the dihedral angle between the foliation in the shale and the FAP first increases and then decreases again. The foliation in the stiffer sandstone exhibits a convergent fan (positive values in Fig. 11b, c) and the foliation orientation almost mirrors that in the shale. In the numerical

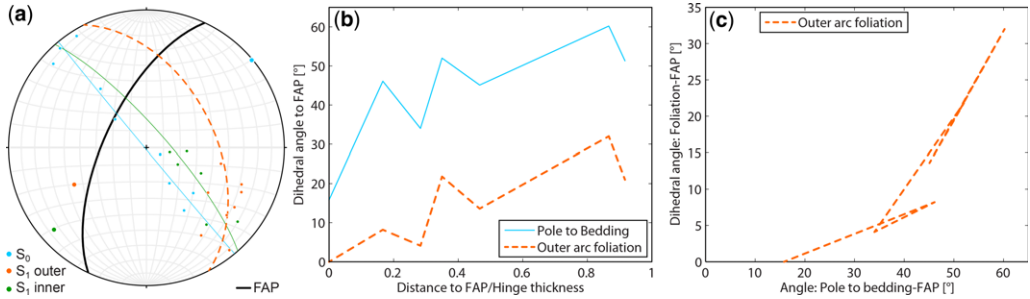


**Fig. 9.** Same as Figure 7 but for field measurements of the outcrop shown in Figure 8. (a)  $S_1$  outer is the foliation at the outer arc of the fold;  $S_1$  inner is the foliation at the inner arc of the fold. (b, c) Only the measurements at the outer arc of the fold are shown.

simulations, similar orientation patterns can be identified for strain measures recording a large amount of strain (e.g. finite strain) or for the passive marker lines in simulations with low viscosity ratios (Fig. 3). This suggests that in the case of the

fold in Figure 10 the foliation started developing early during the folding history and that the mechanical contrast between the quartzite and the shale was not very large during folding. However, the natural data show a large angle between the

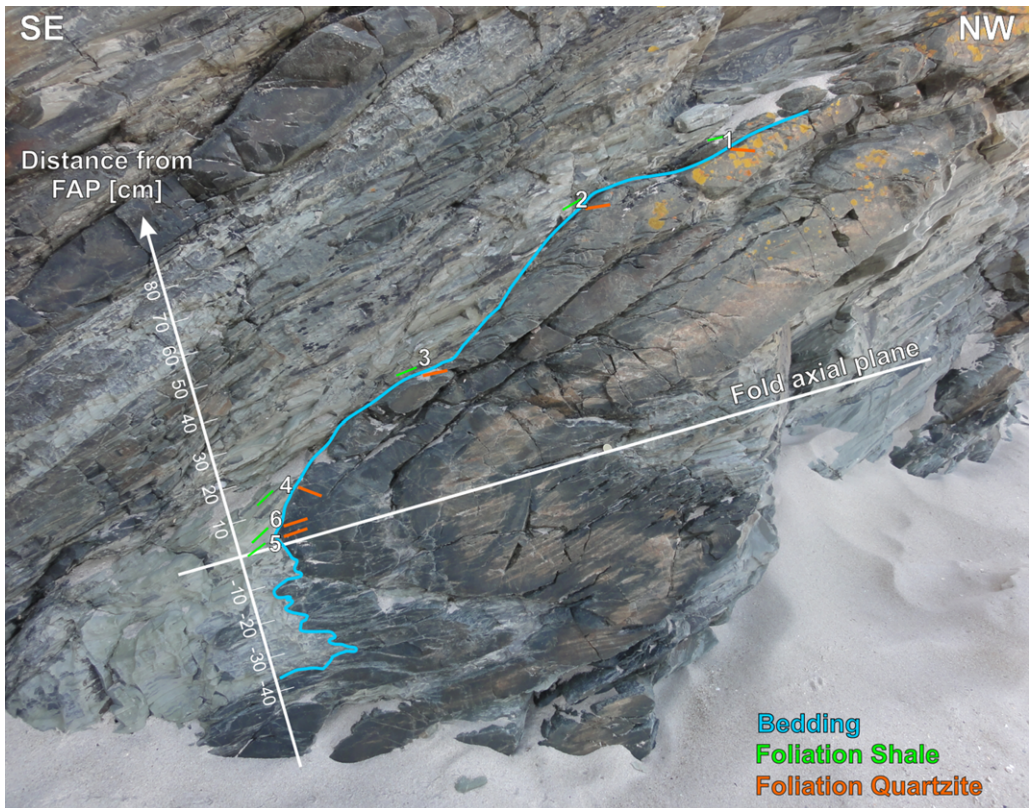


**Fig. 10.** NW-verging, recumbent fold at Benquerencia, developed in quartzitic and shale beds. The bedding interface and foliations in the shale and quartzite layer were measured at the indicated locations. Note the coin in the fold hinge at the inner-fold arc for scale.

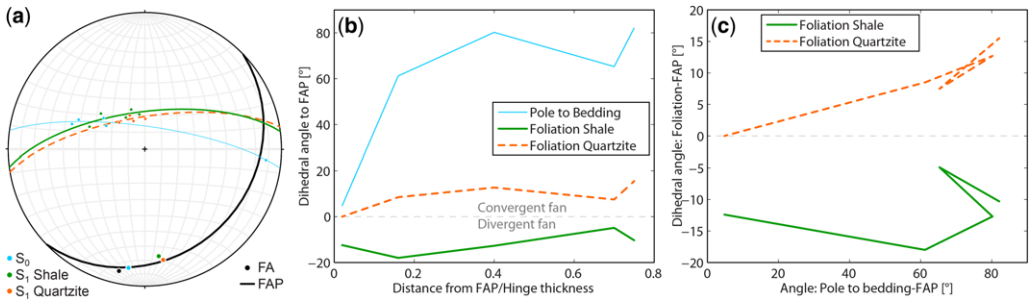


**Fig. 11.** Same as Figure 7 but for field measurements of the outcrop shown in Figure 10. (a)  $S_0$  denotes bedding;  $S_1$  Shale, the foliation in the shale;  $S_1$  Quartzite, the foliation in the quartzite; FA, the measured fold axis; FAP, the measured fold axial plane. In (b) and (c) all the measured data are shown.

pole to bedding and the foliation in the quartzite (mean slope  $< 1$  in Fig. 11c). This is different from the numerical results, for which the major principal strains in the layer are almost layer-perpendicular for strain measures recording large amounts of strain (slope approximately one in Fig. 3b, d).

In all natural cases the foliation in the stiffer folding layer follows the trend of the bedding orientation with various amounts of angular offset. In Figure 7b the angular offset is small and the foliation in the layer is almost perpendicular to the bedding (slope approximately one in Fig. 7c). The orientation of the extensional gashes in Figure 6 also follows the trend of the bedding, but with a larger angular offset than the foliation (Fig. 7b). In the other two natural cases the foliation orientation in the fold has a larger angular offset to the bedding, but still follows the trend of bedding orientation (Figs 9b, c & 11b, c). The numerical results show a similar behaviour but only for strain measures recording a large amount of strain (e.g. finite strain) or for the passive marker lines in the case of small viscosity ratios (Fig. 3). For higher viscosity ratios (Figs 2 & 3c, d) and for strain measures recording smaller amounts of strain, the major principal strains in the folding layer exhibit an almost sudden  $90^\circ$ -switch from a layer-perpendicular orientation close to the synform to a layer-parallel orientation close to the antiform. Such a switch is not observed in the natural folds. One possible interpretation is that all the examined natural folds are characterized by small mechanical contrasts to the surrounding matrix and/or that the foliation in the folds developed very early during the folding history. However, it might also be possible that such a  $90^\circ$ -switch of foliation orientation is not identifiable in the examined folds because the foliation is not developed strongly enough. Also, it has to be emphasized that a layer-parallel foliation is much more challenging to identify as such in the field because it is parallel to the sedimentary

bedding and might be misinterpreted as a sedimentary or diagenetic feature.

One case of layer-perpendicular shortening is present in the fold in Figure 8, at the outermost arc of the fold (inset in Fig. 8). A quartz-filled extensional vein is folded in layer-perpendicular direction and intersected by layer-parallel pressure-solution surfaces. Layer-perpendicular shortening has also been observed in other natural folds, but mainly on the fold limbs. For example, Viola & Mancktelow (2005) observe folding in layer-perpendicular direction of the earlier axial plane foliation on the limbs of metre-scale folds in Namibia. They also describe pressure solution accentuating the existing sedimentary bedding (called pseudobedding in Viola & Mancktelow 2005), which is a manifestation of layer-perpendicular shortening. In Figure 8 the extension gash is clearly older than both its small-scale folding and the pressure solution cutting it and possibly developed due to outer-arc layer-parallel tensional stresses. The younger folding structure of the extension gash and pressure-solution surfaces developed due to layer-perpendicular compression. Both structures indicate that the largest compressive stress acted in layer-perpendicular direction during their formation. In the ideal case of viscous rheology, this corresponds to a layer-parallel orientation of the major principal strain. In the numerical simulations, such orientations are observed for large viscosity ratios (Figs 2 & 3c, d) and for strain measures recording a small amount of strain, and can be explained by the migration of the neutral line from the outer towards the inner arc of the fold (Frehner 2011). Therefore, in contrast to the interpretation above, it may also be inferred that both the quartz vein and the pressure-solution surfaces developed late during the folding history and that the folding layer exhibits a large mechanical contrast to the surrounding matrix. The observed structures would also be promoted by large initial perturbations on the sedimentary

interfaces, as they would lead to faster fold amplification. However, the initial perturbation is almost impossible to estimate in natural folds.

### *Foliation as strain indicator?*

The amount of shortening and the viscosity ratio between layer and matrix can be estimated from the fold shape, using for example the Fold Geometry Toolbox (Adamuszek *et al.* 2011). However, the amount of strain recorded by the foliation is difficult to estimate. The numerical simulations demonstrate that the major principal strain orientations only have small differences for the different strain measures. It is expected that for most natural folds these differences are masked by the natural variations or the errors on measurements of the foliation orientation. In particular, the divergent fan in the matrix around the outer arc of the fold is not very sensitive to the amount of recorded strain for most of the fold (Figs 1–4) and is therefore not a good proxy for strain estimates; on the other hand, the convergent fan in the higher-viscosity layer depends more strongly on the recorded strain (Figs 1 & 4).

When measured exactly at the fold interface, this dependency is not so obvious for all shortening values and viscosity ratios (e.g. dashed lines in Fig. 2e or Fig. 3a, b), but the pattern inside the layer can vary strongly for the different strain measures (Figs 1 & 4). Therefore, it is essential to characterize the entire foliation pattern in natural folds, and not only measure the foliation along the fold interface. Close to the FAP, two perpendicular foliations may overprint each other, because the strain switches by 90° almost instantaneously when the neutral line passes a certain point on the FAP (Frehner 2011). However, this overprinting relationship can be challenging to recognize in natural folds because one of the foliations is bedding-parallel and possibly only weakly developed (e.g. only a few pressure-solution surfaces in the inset in Fig. 8). Other structures (e.g. folded and intersected vein in Fig. 8) can help the interpretation of the 90°-switch of foliation orientation. Especially in areas of polyphase folding or in the absence of additional structures this might be a challenging decision for field geologists. Because of these difficulties, the foliation fan pattern inside the folding layer is also not very well suited as a proxy for strain estimates.

### **Conclusions**

The numerical FE simulations demonstrated that strain measures recording different amounts of strain result in similar refraction patterns to the

major principal strain orientation around buckle folds. In particular the divergent fan pattern in the weak matrix at the outer arc of the folds is nearly insensitive to the amount of strain recorded by the strain measure. Therefore, the divergent foliation fan in the matrix at the outer arc of a natural fold does not necessarily represent the finite strain orientation, but may also represent infinitesimal or an incremental strain. The major principal strain orientation inside the higher-viscosity folding layer is different for the different strain measures, particularly towards the outer arc of the fold, where the strain switches by 90° from a layer-perpendicular to a layer-parallel orientation. Where exactly this 90°-switch happens depends on the external shortening and the amount of strain recorded by the strain measure. However, in the field it can be difficult to identify a layer-parallel foliation because it is parallel to sedimentary or diagenetic structures. Therefore, the foliation fan pattern inside the folding layer is also not very well suited as a proxy for strain estimates.

The natural foliation fan patterns exhibit some of the features observed in the numerical simulations. However, natural orientation variations and noisy data result in foliation orientation plots that are difficult to interpret. No final conclusion can be drawn in terms of the amount of strain that is recorded by the foliation fan patterns as different interpretations are possible. It is expected that a foliation developing early during folding records more strain and resembles the major principal finite strain orientation and that a foliation developing late during folding rather resembles the major principal infinitesimal strain. However, such a one-to-one correlation between natural and numerical data is not possible for the presented case study.

The organizers of the DRT Conference 2011, in particular S. Llana-Fúnez, are acknowledged for their effort in putting together this exciting conference in Oviedo, Spain. A field trip of the authors prior to, and many intense discussions during, the DRT Conference 2011 motivated this work. R. Laner is greatly acknowledged for sharing the scientific findings of his Diploma thesis, as well as for many useful tips on accessible roads and outcrops. This work was supported by the Austrian Science Fund project V151-N22. The referee P. Hudleston is thanked for his constructive criticism of the original manuscript.

### **References**

- ADAMUSZEK, M., SCHMID, D. W. & DABROWSKI, M. 2011. Fold geometry toolbox – Automated determination of fold shape, shortening, and material properties. *Journal of Structural Geology*, **33**, 1406–1416. <http://dx.doi.org/10.1016/j.jsg.2011.06.003>

- ADAMUSZEK, M., SCHMID, D. W. & DABROWSKI, M. 2013. Theoretical analysis of large amplitude folding of a single viscous layer. *Journal of Structural Geology*, **48**, 137–152, <http://dx.doi.org/10.1016/j.jsg.2012.11.006>
- AERDEN, D. G. A. M., SAYAB, M. & BOUYBAOUENE, M. L. 2010. Conjugate-shear folding: a model for the relationships between foliations, folds and shear zones. *Journal of Structural Geology*, **32**, 1030–1045, <http://dx.doi.org/10.1016/j.jsg.2010.06.010>
- BASTIDA, F. & PULGAR, J. A. 1978. La estructura del manto de Mondoñedo entre Burela y Tapia de Casariego (Costa Cantábrica, NW de España). *Trabajos de Geología*, **10**, 75–159.
- BASTIDA, F., MARTINEZ-CATALAN, J. R. & PULGAR, J. A. 1986. Structural, metamorphic and magmatic history of the Mondonedo nappe (Hercynian belt, NW Spain). *Journal of Structural Geology*, **8**, 415–430, [http://dx.doi.org/10.1016/0191-8141\(86\)90060-X](http://dx.doi.org/10.1016/0191-8141(86)90060-X)
- CLOOS, E. 1947. Oolite deformation in South Mountain Fold Maryland. *Geological Society of America Bulletin*, **58**, 843–918, [http://dx.doi.org/10.1130/0016-7606\(1947\)58\[843:ODITSM\]2.0.CO;2](http://dx.doi.org/10.1130/0016-7606(1947)58[843:ODITSM]2.0.CO;2)
- CUVELIER, C., SEGAL, A. & VAN STEENHOVEN, A. A. 1986. *Finite Element Methods and the Navier-Stokes Equations*. D. Reidel Publishing Company, Dordrecht.
- DEBACKER, T. N., VAN NOORDEN, M. & SINTUBIN, M. 2006. Distinguishing syn-cleavage folds from pre-cleavage folds to which cleavage is virtually axial planar: Examples from the Cambrian core of the Lower Palaeozoic Anglo-Brabant Deformation Belt (Belgium). *Journal of Structural Geology*, **28**, 1123–1138, <http://dx.doi.org/10.1016/j.jsg.2006.03.027>
- DIETERICH, J. H. 1969. Origin of cleavage in folded rocks. *American Journal of Science*, **267**, 155–165.
- DIETERICH, J. H. & CARTER, N. L. 1969. Stress-history of folding. *American Journal of Science*, **267**, 129–154.
- FERNÁNDEZ, F. J., ALLER, J. & BASTIDA, F. 2007. Kinematics of a kilometric recumbent fold: The Courel syncline (Iberian massif, NW Spain). *Journal of Structural Geology*, **29**, 1650–1664, <http://dx.doi.org/10.1016/j.jsg.2007.05.009>
- FLETCHER, R. C. 1974. Wavelength selection in the folding of a single layer with power-law rheology. *American Journal of Science*, **274**, 1029–1043.
- FLETCHER, R. C. 1977. Folding of a single viscous layer: Exact infinitesimal-amplitude solution. *Tectonophysics*, **39**, 593–606, [http://dx.doi.org/10.1016/0040-1951\(77\)90155-X](http://dx.doi.org/10.1016/0040-1951(77)90155-X)
- FREHNER, M. 2011. The neutral lines in buckle folds. *Journal of Structural Geology*, **33**, 1501–1508, <http://dx.doi.org/10.1016/j.jsg.2011.07.005>
- FREHNER, M. & SCHMALHOLZ, S. M. 2006. Numerical simulations of parasitic folding in multilayers. *Journal of Structural Geology*, **28**, 1647–1657, <http://dx.doi.org/10.1016/j.jsg.2006.05.008>
- FREHNER, M., REIF, D. & GRASEMANN, B. 2012. Mechanical versus kinematical shortening reconstructions of the Zagros High Folded Zone (Kurdistan region of Iraq). *Tectonics*, **31**, <http://dx.doi.org/10.1029/2011TC003010>
- GROOME, W. G. & JOHNSON, S. E. 2006. Constraining the relative strengths of high-grade metamorphic rocks using foliation refraction angles: an example from the Northern New England Appalachians. *Journal of Structural Geology*, **28**, 1261–1276, <http://dx.doi.org/10.1016/j.jsg.2006.03.023>
- HAUGHTON, S. 1856. On slaty cleavage and the distortion of fossils. *Philosophical Magazine*, **12**, 409–421.
- HAUPT, P. 2002. *Continuum Mechanics and Theory of Materials*. Springer Verlag, Berlin.
- HUDLESTON, P. J. & LAN, L. 1993. Information from fold shapes. *Journal of Structural Geology*, **15**, 253–264, [http://dx.doi.org/10.1016/0191-8141\(93\)90124-S](http://dx.doi.org/10.1016/0191-8141(93)90124-S)
- HUDLESTON, P. J. & LAN, L. 1995. Rheological information from geological structures. *Pure and Applied Geophysics*, **145**, 605–620, <http://dx.doi.org/10.1007/BF00879591>
- HUDLESTON, P. J. & TREAGUS, S. H. 2010. Information from folds: a review. *Journal of Structural Geology*, **32**, 2042–2071, <http://dx.doi.org/10.1016/j.jsg.2010.08.011>
- HUGHES, T. J. R. 2000. *The Finite Element Method: Linear Static and Dynamic Finite Element Analysis*. Dover Publications, Mineola.
- LAN, L. & HUDLESTON, P. J. 1995. The effects of rheology and the strain distribution in single layer buckle folds. *Journal of Structural Geology*, **17**, 727–738, [http://dx.doi.org/10.1016/0191-8141\(94\)00095-H](http://dx.doi.org/10.1016/0191-8141(94)00095-H)
- LANER, R. 2010. *Fluid assisted cataclastic deformation in quartzitic rocks (Portizuelo Antiforme, Luarca, NW Spain)*. Master thesis, Faculty of Earth Sciences, Geography and Astronomy, University of Vienna (Austria), [http://othes.univie.ac.at/10591/1/2010-07-14\\_9725921.pdf](http://othes.univie.ac.at/10591/1/2010-07-14_9725921.pdf)
- LECHMANN, S. M., SCHMALHOLZ, S. M., BURG, J.-P. & MARQUES, F. O. 2010. Dynamic unfolding of multilayers: 2D numerical approach and application to turbidites in SW Portugal. *Tectonophysics*, **494**, 64–74, <http://dx.doi.org/10.1016/j.tecto.2010.08.009>
- MANCKTELOW, N. S. 2001. Single layer folds developed from initial random perturbations: the effects of probability distribution, fractal dimension, phase and amplitude. In: KOYI, H. A. & MANCKTELOW, N. S. (eds) *Tectonic Modeling: A Volume in Honor of Hans Ramberg*. Geological Society of America Memoirs, Boulder, **193**, 69–87.
- MARCOS, A. 1973. Las Series del Paleozoico Inferior y la estructura herciniana del occidente de Asturias (NW de España). *Trabajos de Geología*, **6**, 1–113.
- MULCHRONE, K. F. & MEERE, P. A. 2007. Strain refraction, viscosity ratio and multi-layer deformation: a mechanical approach. *Journal of Structural Geology*, **29**, 453–466, <http://dx.doi.org/10.1016/j.jsg.2006.10.004>
- OERTEL, G. 1983. The relationship of strain and preferred orientation of phyllosilicate grains in rocks – a review. *Tectonophysics*, **100**, 413–447, [http://dx.doi.org/10.1016/0040-1951\(83\)90197-X](http://dx.doi.org/10.1016/0040-1951(83)90197-X)
- OERTEL, G., ENGELDER, T. & EVANS, K. 1989. A comparison of the strain of crinoid columnals with that of their enclosing silty and shaly matrix on the Appalachian Plateau, New York. *Journal of Structural Geology*, **11**, 975–993, [http://dx.doi.org/10.1016/0191-8141\(89\)90048-5](http://dx.doi.org/10.1016/0191-8141(89)90048-5)

- PRICE, N. J. & COSGROVE, J. W. 1990. *Analysis of Geological Structures*. Cambridge University Press, Cambridge.
- RAMSAY, J. G. 1967. *Folding and Fracturing of Rocks*. McGraw-Hill Book Company, New York.
- RAMSAY, J. G. & HUBER, M. I. 1987. *The Techniques of Modern Structural Geology, Volume 2: Folds and Fractures*. Academic Press, London.
- REBER, J. E., SCHMALHOLZ, S. M. & BURG, J.-P. 2010. Stress orientation and fracturing during three-dimensional buckling: Numerical simulation and application to chocolate-tablet structures in folded turbidites, SW Portugal. *Tectonophysics*, **493**, 187–195, <http://dx.doi.org/10.1016/j.tecto.2010.07.016>
- SHARPE, D. 1847. On slaty cleavage. *Quarterly Journal of the Geological Society of London*, **3**, 74–105.
- SHIMAMOTO, T. & HARA, I. 1976. Geometry and strain distribution of single-layer folds. *Tectonophysics*, **30**, 1–34, [http://dx.doi.org/10.1016/0040-1951\(76\)90135-9](http://dx.doi.org/10.1016/0040-1951(76)90135-9)
- SIDDANS, A. W. B. 1972. Slaty cleavage: a review of research since 1815. *Earth-Science Reviews*, **8**, 205–232.
- SORBY, H. C. 1853. On the origin of slaty cleavage. *Edinburgh New Philosophical Journal*, **55**, 137–148.
- TALBOT, C. J. 1999. Can field data constrain rock viscosities? *Journal of Structural Geology*, **21**, 949–957, [http://dx.doi.org/10.1016/S0191-8141\(99\)00037-1](http://dx.doi.org/10.1016/S0191-8141(99)00037-1)
- TREAGUS, S. H. 1983. A theory of finite strain variation through contrasting layers, and its bearing on cleavage refraction. *Journal of Structural Geology*, **5**, 351–368, [http://dx.doi.org/10.1016/0191-8141\(83\)90023-8](http://dx.doi.org/10.1016/0191-8141(83)90023-8)
- TREAGUS, S. H. 1988. Strain refraction in layered systems. *Journal of Structural Geology*, **10**, 517–527, [http://dx.doi.org/10.1016/0191-8141\(88\)90038-7](http://dx.doi.org/10.1016/0191-8141(88)90038-7)
- TREAGUS, S. H. 1999. Are viscosity ratios of rocks measurable from cleavage refraction? *Journal of Structural Geology*, **21**, 895–901, [http://dx.doi.org/10.1016/S0191-8141\(99\)00018-8](http://dx.doi.org/10.1016/S0191-8141(99)00018-8)
- TREAGUS, S. H. & SOKOUTIS, D. 1992. Laboratory modeling of strain variations across rheological boundaries. *Journal of Structural Geology*, **14**, 405–424, [http://dx.doi.org/10.1016/0191-8141\(92\)90102-3](http://dx.doi.org/10.1016/0191-8141(92)90102-3)
- TULLIS, T. E. & WOOD, D. S. 1975. Correlation of finite strain from both reduction bodies and preferred orientation of mica in slate from Wales. *Geological Society of America Bulletin*, **86**, 632–638, [http://dx.doi.org/10.1130/0016-7606\(1975\)86<632:COFSFB>2.0.CO;2](http://dx.doi.org/10.1130/0016-7606(1975)86<632:COFSFB>2.0.CO;2)
- TWISS, R. J. & MOORES, E. M. 2007. *Structural Geology* 2nd edn. H. W. Freeman & Company, New York.
- VIOLA, G. & MANCKTELOW, N. S. 2005. From XY tracking to buckling: axial plane cleavage fanning and folding during progressive deformation. *Journal of Structural Geology*, **27**, 409–417, <http://dx.doi.org/10.1016/j.jsg.2004.10.011>
- WOOD, D. S. 1973. Patterns and magnitudes of natural strain in rocks. *Philosophical Transactions of the Royal Society London A – Mathematical Physical and Engineering Sciences*, **274**, 373–382, <http://dx.doi.org/10.1098/rsta.1973.0066>
- WOOD, D. S. 1974. Current views of the development of slaty cleavage. *Annual Reviews of Earth and Planetary Sciences*, **2**, 369–401.
- WOOD, D. S. & OERTEL, G. 1980. Deformation in the Cambrian Slate Belt of Wales. *Journal of Geology*, **88**, 309–326.
- ZIENKIEWICZ, O. C. & TAYLOR, R. L. 2000. *The Finite Element Method, Volume 1: The Basis*. Butterworth-Heinemann, Oxford.